Phonon-Suppressed Auger Scattering of Charge Carriers in Defective Two-Dimensional Transition Metal Dichalcogenides

Linqiu Li,[†,∇] Ming-Fu Lin,[‡,∇] Xiang Zhang,[§] Alexander Britz,[‡,∥] Aravind Krishnamoorthy,[⊥] Ruru Ma,[⊥] Rajiv K. Kalia,[⊥] Aiichiro Nakano,[⊥] Priya Vashishta,[⊥] Pulickel Ajayan,[§] Matthias C. Hoffmann,[‡] David M. Fritz,[‡] Uwe Bergmann,*[,∥] and Oleg V. Prezhdo*[,†,#]

[†]Department of Chemistry, University of Southern California, Los Angeles, California 90089, United States

[‡]Linac Coherent Light Source, SLAC National Accelerator Laboratory, Menlo Park, California 94025, United States

[§]Department of Materials Science and Nanoengineering, Rice University, Houston, Texas 77005, United States

[∥]Stanford PULSE Institute, SLAC National Accelerator Laboratory, Menlo Park, California 94025, United States

[⊥]Collaboratory for Advanced Computing and Simulations, Department of Physics &Astronomy, Department of Computer Science, Department of Chemical Engineering & Materials Science, Department of Biological Sciences, University of Southern California, Los Angeles, California 90089, United States

[#]Department of Physics & Astronomy, University of Southern California, Los Angeles, California 90089, United States

S Supporting Information

ABSTRACT: Two-dimensional transition metal dichalcogenides (TMDs) draw strong interest in materials science, with applications in optoelectronics and many other fields. Good performance requires high carrier concentrations and long lifetimes. However, high concentrations accelerate energy exchange between charged particles by Auger-type processes, especially in TMDs where many-body interactions are strong, thus facilitating carrier trapping. We report time-resolved optical pump-THz probe measurements of carrier lifetimes as a function of carrier density. Surprisingly, the lifetime reduction with increased density is very weak. It decreases only by 20% when we increase the pump fluence 100 times. This unexpected feature of the Auger process is rationalized by our time-domain *ab initio* simulations. The simulations show that phonon-driven trapping competes successfully with the Auger process. On the one hand, trap states are relatively close to band edges, and phonons accommodate efficiently the electronic energy during the trapping. On the other hand, trap states localize around defects, and the overlap of trapped and free carriers is small, decreasing carrier−carrier interactions. At low carrier densities, phonons provide the main charge trapping mechanism, decreasing carrier lifetimes compared to defect-free samples. At high carrier densities, phonons suppress Auger processes and lower the dependence of the trapping rate on carrier density. Our results provide theoretical insights into the diverse roles played by phonons and Auger processes in TMDs and generate guidelines for defect engineering to improve device performance at high carrier densities.

KEYWORDS: transition metal dichalcogenides, Auger process, phonons, carrier density
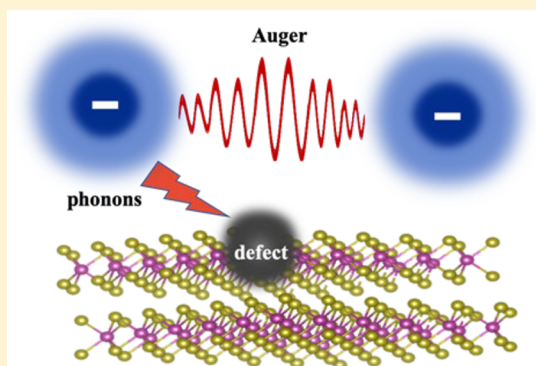
Two-dimensional transition metal dichalcogenides (TMDs) of the general formula MX_2, where M = Mo, W and X = S, Se, Te, have unique properties that have drawn intense interest in materials science and solid-state physics.[1−6] Unlike conventional 3D materials, where surface termination of a crystal lattice results in dangling bonds, TMDs have natural out-of-plane self-termination.[7] TMDs possess other important properties, such as significant photoluminescence efficiency of high quality samples at the monolayer limit, large charge carrier mobility, high current carrying capacity, strong catalytic activity, and good mechanical flexibility.[8−13] Their unique chemical, electrical, mechanical and optical features,

and potential for applications have stimulated an explosive growth in research efforts.[14−17]

Because of their unique optical and electric properties, TMDs are promising building blocks for a new generation of optoelectronics. However, the reported photoluminescence quantum efficiencies of as-grown TMD materials are typically in the range from 10^{-4} to 10^{-2}, which limits their applications in realistic devices.[18] Deterioration of the radiative quantum efficiency is attributed to charge scattering off short-range

disorder defects, such as vacancies, antisites, and adatoms. Chalcogen vacancy defects are frequently observed in chemical vapor deposition (CVD) grown TMD samples, and previous theoretical studies show that the vacancy accelerates charge carrier recombination nonradiatively.[19,20] Later Bajar et al. found that chalcogen vacancies are passivated by oxygen atoms.[21] However, midgap trap states are commonly observed in TMDs.[22−28] Even when chalcogen vacancies are passivated by oxygen, O_2 molecules can embed into defect sites to form Te−O and Mo−O bonds, which also create midgap states.[29] Here, we use Te vacancy as the model system to study the general TMDs midgap defective systems. In addition to the direct energy losses to phonons as shown in Figures 1(a,b), the
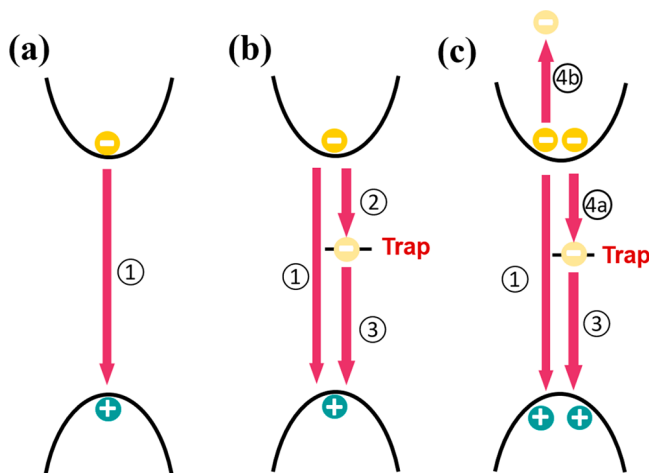

Figure 1. Schematics of charge carrier energy loss to phonons in (a) a pristine TMD crystal and (b,c) a defective TMD crystal with trap levels residing inside the band gap. After photoexcitation, excited electrons in the conduction band (CB) recombine nonradiatively with holes in the valence band (VB) through channel ①, phonon-driven channel. Defects generate trap states within the bandgap. A fraction of photoexcited electrons gets trapped through channel ② and recombines with the VB holes ③. Auger-type carrier trapping takes place at high carrier densities, as shown in channel ④ (i.e., one electron is trapped, denoted as 1st electron, while the other electron is excited into deep CB, denoted as 2nd electron). Electron and hole are displayed in yellow and emerald, respectively. Red arrows represent electron relaxation in the energy domain.

strong quantum confinement and reduced dimensionality of TMDs significantly enhance many-body interactions, which facilitates energy exchange between charge carriers and enables efficient Auger recombination,[30,31] as displayed in Figure 1(c). For example, rapid Auger-type annihilation has been detected in photoexcited MoS_2.[32]

In addition to the recombination dynamics, fast charge trapping is widely detected in TMDs on a 1−2 ps time scale.[33−37] Wang et al. and Kar et al. attribute these fast dynamics to Auger trapping of free carriers.[33−35] Defects in TMDs introduce midgap states that can trap electrons from CB and utilize the released energy to excite free CB electrons to higher energy states. Surprisingly, these fast dynamics are nearly independent of the pump fluence, which contradicts relaxation by the Auger mechanism. Since Auger processes involve scattering between two or more charge carriers, the rate of Auger trapping should grow as the pump fluence increases since more charge carriers are produced at higher fluences. Meanwhile, phonon-driven trapping is independent

of pump fluence because it involves scattering of individual carriers by phonons. For this reason, Xing et al. and Docherty et al. believe these fast dynamics are driven by phonons.[36,37] However, on the one hand, our previous calculations show that purely phonon-driven trapping of charge carriers takes longer time.[19,38] On the other hand, Auger processes can become quite important at high carrier densities, as more carriers can be involved in the dynamics. Therefore, it is not yet known whether these fast dynamics are phonon-driven or Auger-driven or whether both mechanisms are influential. A detailed understanding of the interplay between the Auger-type and phonon-driven charge trapping processes is still lacking. Kinetic rate equations could provide simple models of the charge carrier dynamics. A thorough atomistic understanding of interactions between carriers, phonons, and traps requires an *ab initio* level of description.

In this Letter, we employ time-domain *ab initio* calculations to rationalize our time-resolved optical pump and THz probe transient absorption measurements on charge carrier trapping in multilayer $MoTe_2$, performed in the high carrier density regime with the densities ranging from $\sim 10^{19}$ to 10^{21} cm^{-3}. We observe only a very weak dependence of the charge carrier lifetime on the carrier density. This fact is surprising since straightforward models predict quadratic density dependence of charge−charge scattering. The observation is explained by our time-domain *ab initio* simulations of charge carrier dynamics in defective $MoTe_2$. The simulations show that, first, charge trapping facilitated by phonons is already quite fast but still cannot explain our observations. Second, charge trapping via Auger-type carrier−carrier scattering is strongly influenced by phonons. The excited carrier in the Auger process accepts about 50% of the trapped carrier energy, with more than half of the energy dissipated directly to phonons. The Auger-type mechanism accelerates the carrier trapping by a factor of 4, and the simultaneous phonon-driven and Auger-type trapping occurs within ∼2 ps, in agreement with the experimental results. Phonons participate strongly because trap states are relatively shallow, and phonons accommodate efficiently the electronic energy loss during the trapping. Trapped electrons localize around defects, decreasing the overlap of wave functions between trapped and free carriers, and reduce carrier−carrier scattering. Thus, phonons-driven electron trapping suppresses the Auger mechanism at high carrier densities and lowers the dependence of the carrier lifetime on the carrier density. Our time-domain atomistic modeling is consistent with the unexpected experimental trend and provides a detailed analysis of the strongly coupled charge−phonon and charge−charge scattering processes that are common to a majority of nanoscale materials.

Transient absorption measurements using terahertz (THz) pulses provide a direct probe of photoconductivity in a material induced by the optical excitation. Photoconductivity is a product of free carrier mobility and concentration. Thus, it is a sensitive measurement of free charges.[39−42] In these experiments, we characterize the THz field transmitted through the sample at each pump−probe delay step and convert the obtained THz field in the time domain to the spectral domain. The procedure allows us to catch the short-lived carrier lifetime without the complication of the THz field phase drift at a single point measurement of the maximum field. The THz apparatus and data analysis are detailed in Sections II and III of the Supporting Information (SI), respectively. Optical excitation at 800 nm (1.55 eV) is
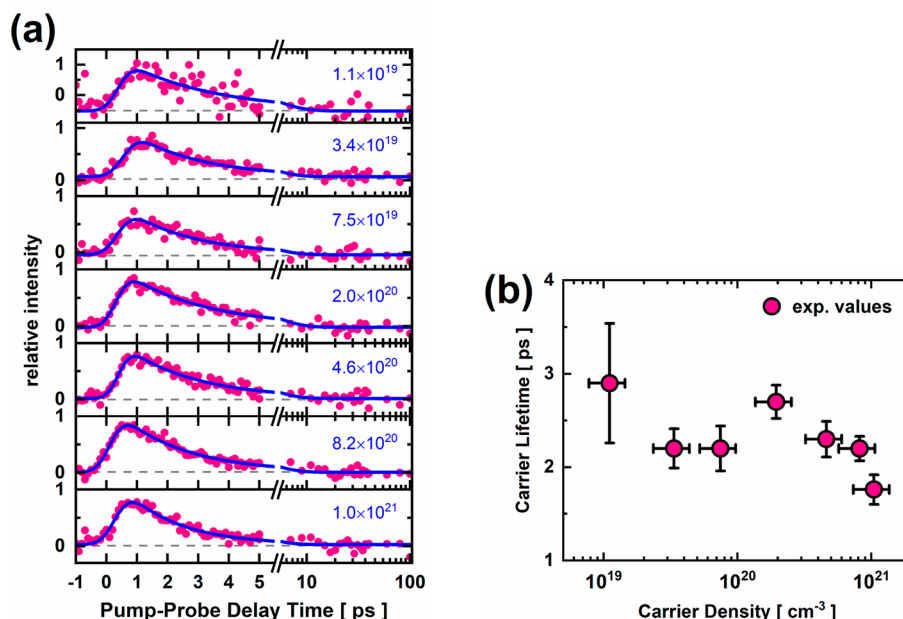
Figure 2. Optical pump and THz probe measurements of ~9 nm thick 2H-phase $MoTe_2$. The THz probe beam is normal incident to the sample surface, and the transmitted THz field is measured by the electro-optic sampling method. (a) The kinetics plots of 2H-phase $MoTe_2$ after optical excitation at 800 nm. These plots are obtained from the integration of normalized THz spectral intensity change from 0.5 to 2.3 THz (see Supporting Information IV for more details). Red dots and blue lines represent the experimental results and overall fits, respectively. Each fit is obtained by considering a convolution of instrumental response function of ~0.3 ps with an exponential decay function. The carrier density shown in the plots increases toward the bottom by a factor of ~100. Note that the unit for the carrier density is in cm^{-3}. (b) The time constants obtained from the fits in (a) as a function of carrier density. The horizontal error bars in the figure represent the measured uncertainties of pulse energy and pump beam spot size. The vertical error bars in the lifetime correspond to the uncertainty obtained from the least-squared fit of the experimental data points.

employed to generate free carriers over the band edge of $MoTe_2$. The sample preparation and characterization of multilayered $MoTe_2$ polycrystalline are presented in Section I of the SI.[43] Note that at high pump fluences in this experiment, the generated excitons dissociate into free carriers.[44] The estimated Mott density for exciton dissociation to occur is at ~10^{18} cm^{-3} based on the Mott criterion $N_{Mott} = (0.25/a_{Bohr})^3$, where a_{Bohr} is the Bohr radius of exciton in bulk 2H-phase $MoTe_2$ (i.e., 2.5 nm).[45] The pump–probe kinetics at different effective carrier densities are shown in Figure 2(a), with the charge carrier density increasing from top to bottom by over a factor of ~100. The red and blue curves represent the experimental results and best least-squares-fits, respectively. Each fit is performed with inclusion of a convolution between the instrument response function of ~0.3 ps and the exponential decay function. The obtained lifetimes as a function of carrier density are plotted in Figure 2(b). Note that each carrier density is calculated by considering the complex refractive indices of air, $MoTe_2$, and substrates at 800 nm photon energy. This allows us to estimate the absorption of photons taking into account the reflection at the interfaces between air, $MoTe_2$, and substrates.[46] Finally, the saturation effect at high pump fluence is included so that the actual absorption correction can be estimated from saturable absorber model. In addition, we assume that each photon produces one electron–hole pair that dissociates into free carriers. Detailed estimation of carrier density is shown in Supporting Information IV.

Our experimental results display ~2 to 3 ps free charge carrier lifetimes in 13-layered $MoTe_2$ at the carrier density from ~10^{19} to 10^{21} cm^{-3} as shown in Figure 2(b). The picosecond lifetimes suggest that the observed dynamics may not be simply attributed to the intraband relaxation of hot carriers to the band edge via phonon emission because such process occurs on a much shorter time scale, 100 to 500 fs, and thus, it can be excluded.[47,48] However, this 2 ps time scale of carrier dynamics may be attributed to the interplay between the electron−phonon scattering and Auger trapping processes by the defect states.[35,37,49] Once the free carriers are trapped, the photoconductivity decays to zero.[35,37,50] Afterward, the trapped carriers recombine nonradiatively, which is invisible to the THz field. Note that the exciton contribution in our THz signal is negligible because the intraexcitonic transition requires ~20 to 50 meV, which is outside of our THz-probe region (2 to 12 meV). In addition, at current excitation densities the excitons fully dissociate into free carriers based on Mott density estimation using the exciton Bohr radius in the bulk $MoTe_2$. The two-dimensional nature of $MoTe_2$ enhances many-body interactions, and at our current carrier density the Auger process becomes efficient, as observed in a few-layer MoS_2.[33,51]

In Figure 2(b), the measured dependence of the charge carrier lifetimes on the charge carrier density is weak. Considering a two-particle scattering event, one expects quadratic dependence of carrier lifetime on the particle density, and the lower than quadratic dependence on the charge carrier density is surprising. The carrier lifetimes also depend on the density of trap states, Figure 1(c). The defect density is maintained constant in our experiments since we use the same prepared 9 ± 1.1 nm thick polycrystalline $MoTe_2$ samples while varying the pump intensity. Note that the pump fluence that generates the highest carrier density in the current

study is two times smaller than the damage threshold of $MoTe_2$ samples. A subquadratic carrier density dependence can arise if trapping is purely an electron−phonon scattering event, and charge−charge scattering is rare. However, this is unlikely for the high carrier densities used in our experiments. Most likely, the Auger process occurs simultaneously with phonon-driven trapping, and the Auger scattering is accompanied by charge−phonon scattering of the same type that leads to the subpicosecond intraband charge−phonon relaxation.[47,48] An interplay between Auger and phonon scattering has been established, for instance, during multiple exciton generation[52,53] and Auger-assisted electron transfer[54,55] in semiconductor quantum dots (QD). Note that compared to the TMDs, QDs show stronger confinement, but weaker Coulomb interactions due to 3D screening over the QD volume. The observed 2 to 3 ps time scale as observed in Figure 2 cannot be attributed to direct nonradiative charge recombination in TMDs, which requires much longer time (i.e., ∼23 ps).[33,51]

In order to rationalize the weak dependence of the charge carrier lifetime on the carrier density in $MoTe_2$ we performed time-domain *ab initio* simulations combining real-time time-dependent (TD) density functional theory (DFT) with nonadiabatic (NA) molecular dynamics (MD). The electron and phonon dynamics are directly coupled in the simulation. The $MoTe_2$ structure, including a Te vacancy defect to create midgap states, is represented at the atomistic level, and vibrations are described fully anharmonically, which is important for modeling defect modes. Experiments detected the common existence of vacancy defects in chemical vapor grown TMDs samples,[1,20,56] motivating our model. Among all point defects, one chalcogen vacancy is calculated to have the lowest formation energy.[20] It is reported that oxygen could passivate vacancy defects and recover the no midgap band structure.[21] However, oxygen can further interact with the Mo vacancy to create new midgap states.[50] Since vacancies are common and widely studied defects in TMDs, we use chalcogen vacancy as a model to represent defective systems with midgap states. Charge carriers can also relax into exciton levels. However, the experimental pump fluences are high, and excitons dissociate into free carriers. Only at low pump fluences, or at later stages of the carrier relaxation at high pump fluences, excitons can provide an efficient channel for carrier trapping.

We used a bilayer $MoTe_2$ in the simulation to mimic the charge trapping dynamics in the 14-layered $MoTe_2$ used in the experiments. While monolayer $MoTe_2$ is a direct bandgap semiconductor, bilayer $MoTe_2$ already has an indirect bandgap, similarly to multilayer $MoTe_2$, and the corresponding photoluminescence intensity is low compared to the monolayer.[16,57] Our Raman spectrum of $2H\text{-}MoTe_2$ shows similar features and intensity as observed from previous bilayer studies.[16] The TDDFT-NAMD quantum dynamics simulations are computationally intense, involving several thousand nuclear time-steps, each requiring an electronic structure calculation and hundreds of thousands electronic time-steps. The bilayer $MoTe_2$ model demands significantly less computational cost than multilayer $MoTe_2$, making it applicable at the *ab initio* level. The bilayer model already captures the overall trend and rationalizes the experimental data.

The DFT calculations and adiabatic MD are performed with the Quantum Espresso program.[58] The TDDFT and NAMD simulations are carried out with the Pyxaid software package-

age.[59,60] The phonon-driven nonradiative charge trapping and recombination are simulated using the decoherence-induced surface hopping (DISH) method.[61] DISH has been used to model excited state dynamics in closely related TMDs systems, such as MoS_2 monolayers and MoS_2/WS_2 and $MoS_2/MoSe_2$ heterojunctions.[19,38,62−64] Auger-mediated dynamics are computed with the global-flux surface hopping (GFSH) method.[65] GFSH captures many-particle processes and has been successful in simulating Auger processes in semiconductor QDs, nanoplatelets, and nanotubes.[66−68] This is the first study of Auger-type dynamics in TMDs. Simulation details are provided in Section V of the SI.

Figure 3 depicts the simulated structure and densities of states (DOS) of the pristine and defective $MoTe_2$ bilayers. The
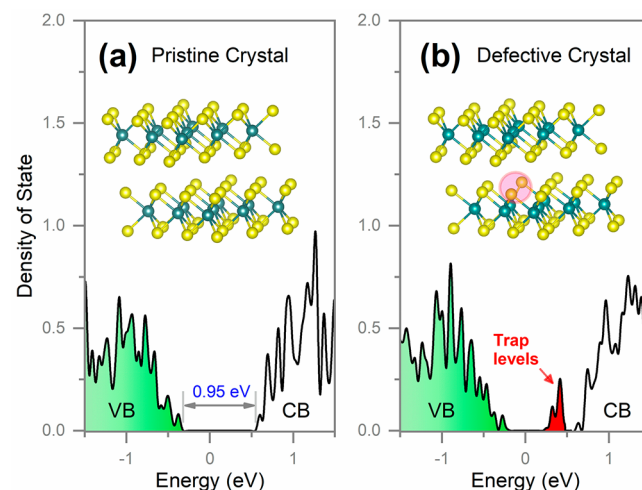

Figure 3. Structures, top, and density of states (DOS), bottom, of (a) pristine $MoTe_2$ bilayer with calculated band gap of 0.95 eV between valence band maximum (VBM) and conduction band minimum (CBM), and (b) $MoTe_2$ bilayer with one Te vacancy (V_{Te}). The vacancy is denoted with a red circle. It creates electrons traps within the bandgap, as are shown in the red area in the bottom. The energy of trap states locates approximately 0.2 to 0.3 eV below the CBM. Emerald and yellow balls represent Mo and Te atoms, respectively.

calculated bandgap of the pristine $MoTe_2$ bilayer is 0.95 eV, which agrees with the previous experimental and theoretical results within ∼0.1 eV.[16,69] The Te vacancy creates two trap levels residing approximately ∼0.2 to 0.3 eV below the conduction band minimum (CBM) as shown in Figure 3(b). The relatively small energy gap between the CBM and the trap states suggests fast electron trapping dynamics. The vacancy of Te in the crystal (V_{Te}) creates unsaturated chemical bonds at Mo atoms, and the compromised lattice structure allows for larger amplitude, anharmonic motions near the defect site. The defect perturbs symmetry of the $MoTe_2$ bilayer, giving rise to vibrational modes that are not originally available in the defect-free system, and accelerates nonradiative charge carrier relaxation. By creating a single point vacancy within the 3 × 3 supercell of the $MoTe_2$ bilayer, we generate a high defect concentration of 8.3×10^{20} cm^{-3} in the crystal (i.e., 9.0×10^{13} cm^{-2} per layer). This defect concentration is similar to the experimental value of ∼3.5×10^{13} cm^{-2} determined for monolayer MoS_2 synthesized by CVD.[1] In addition, by placing two charges in this supercell we create a high carrier density of ∼10^{21} cm^{-3}, which is falling within the experimental range, Figure 2(b).

Next, we simulate phonon-driven charge carrier recombination and trapping in the pristine and defective $MoTe_2$ bilayers, respectively, based on the processes ① and ② in Figures 1(a,b), without considering the Auger effect. Figure 4 presents the
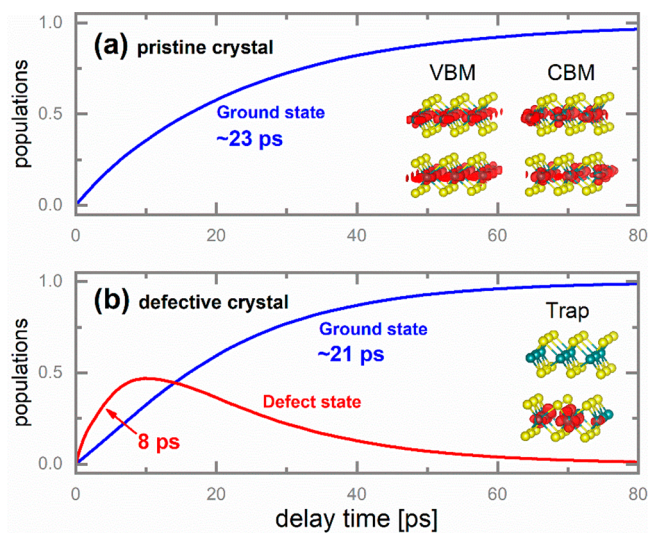

Figure 4. Simulations of phonon-induced charge carrier recombination and trapping dynamics in (a) pristine $MoTe_2$ bilayer based on the model shown in Figure 1(a,b) $MoTe_2$ bilayer with tellurium vacancy, V_{Te}, based on the model shown in Figure 1(b). Only a single electron–hole pair is present in this simulation, and Auger processes are not allowed. The recovery of the ground state (GS) population, shown by the blue lines, occurs on a ∼ 20 ps time scale in both systems. For a defective bilayer, V_{Te} creates electron traps located at ∼0.2 to 0.3 eV below the CBM. Carrier relaxation through the trap level is shown by the red curve. Electrons are quickly trapped in the defect levels within ∼8 ps and recombine with holes at VBM at later time. The insets in (a) show charge densities of the VBM and CBM, and in (b) the higher energy defect state. Both VBM and CBM delocalize throughout the whole bilayer, while the electron trap resides locally around the defect and within one layer.

simulated time-resolved populations of the electronic states involved in the charge carrier relaxation dynamics. The insets show charge densities of the VBM and CBM in Figure 4(a) and trap states in Figure 4(b), respectively. The time scales presented in the figure are obtained through exponential fittings of the simulation data. The ground state recovery in the pristine system takes ∼23 ps, which is still one order of magnitude slower than our experimental observation. It is important to note that the simulation described in Figure 4 only allows phonon-driven nonradiatively processes. Thus, the results of Figure 4 mimic high carrier density experiments in which Auger-type charge–charge scattering is turned off.

The phonon-driven nonradiative charge carrier recombination, channel ①, accelerates slightly in the presence of the V_{Te} defect as shown in the blue curve in Figure 4(b). The electron is trapped from the CB into the defect states within a few picoseconds and then proceeds to recombine with the hole in the VB (red curve in Figure 4(b)). The fast rise of the defect level population, compared to the ∼21 ps ground state recovery time, and the relatively large transient amplitude of the defect population, nearly 50%, indicating a significant contribution of carrier relaxation through the defect level. This conclusion is confirmed further by the values of the nonadiabatic coupling (NAC) presented in Table 1. Defined

Table 1. Root-Mean-Square Nonadiabatic Coupling (NAC) for Charge Carrier Trapping and Recombination Processes

	pristine bilayer	defective bilayer with V_{Te}		
	recombination of CB (e⁻) and VB (h⁺)	recombination of CB (e⁻) and VB (h⁺)	VBM to trap	CBM to trap
NAC (meV)	4.54	3.88	4.89	4.63
energy gap (eV)	0.95	0.95	0.65–0.75	0.2–0.3

as $\left\langle i\hbar\Phi_j|\nabla_{\mathbf{R}}|\Phi_k\cdot\frac{d\mathbf{R}}{dt}\right\rangle$, see Section VI of the SI, the NAC depends on the overlap of wave functions of initial and final electronic states , and reflects the sensitivity of the wave functions to nuclear movements. The NAC is a form of electron–phonon coupling. The NACs from the trap level to the CBM and VBM are ∼20% larger than the NAC of carriers between the CBM and VBM. It is important to note that the calculated charge carrier lifetimes in $MoTe_2$ are shorter than in other TMDs systems.[22] This is because $MoTe_2$ has a significantly smaller band gap than other TMDs, such as $MoSe_2$ and MoS_2. The carrier recombination in defective $MoTe_2$ is reported to be ∼60 ps, which is consistent with our results.[70]

The ∼8 ps time of phonon-mediated electron trapping is a factor of two to three larger than the experimentally determined carrier trapping times as displayed in Figure 2(b). This is because the simulation described in Figure 4 does not allow for Auger-type carrier–carrier energy exchange, which is actually happening in the experiment at high carrier densities. Next we turn on the Auger channel and simulate simultaneous phonon-mediated and Auger-mediated electron trapping, and the results are shown in Figure 5. Figure 1 illustrates three different mechanisms of charge carrier relaxation, among which the third mechanism including both Auger and phonon-driven processes is consistent with our THz results.

Figures 5(a,c) compare electron trapping driven purely by phonons, channel ② in Figure 1(b), with electron trapping driven by both phonons and electron–electron energy exchange, channel ④ in Figure 1(c), respectively. Note that the hole is not present in the current simulation so that the blue curve in Figure 5(a) does not decay to zero as was observed in the red curve in Figure 4(b). This allows us to reduce computational expense significantly while maintaining the accuracy of simulation for nonradiative carrier relaxation process to the trap levels. The simulation includes trap states and 30 CB states for each of the two electrons, giving a 32 × 32 = 1024 state basis for quantum dynamics. Adding another 30 VB states for the hole would increase the many-particle basis to ∼30,000, greatly increasing the computational cost. Thus, Auger-type energy exchange occurs between the two electrons present in the simulation. The simulation already captures the essential physics and allows not only the pure Auger scattering but also Auger scattering that occurs simultaneously with charge–phonon relaxation.

Figure 5(a) matches well the rise of the trap state population in Figure 4(b), both processes corresponding to phonon-mediated electron trapping. The key result of the present work is demonstrated in Figures 5(c,d). Figure 5(c) shows that Auger-type electron–electron scattering accelerates the charge
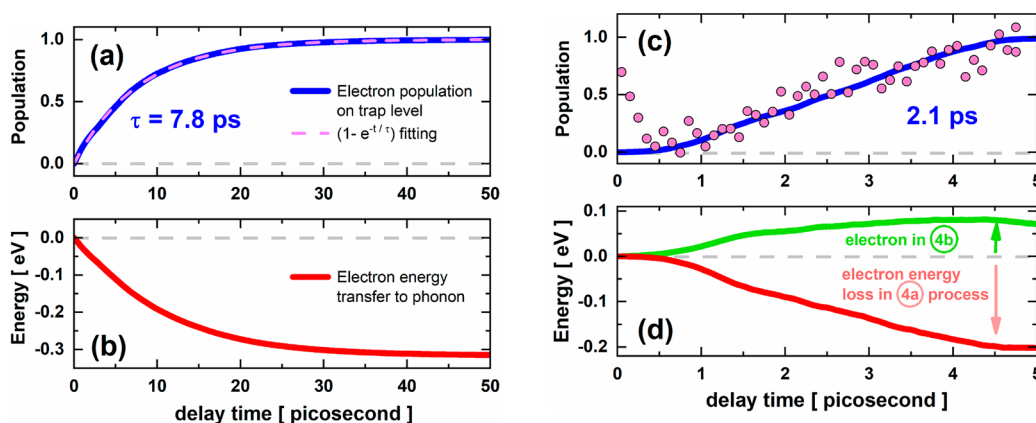
Figure 5. Simulations of electron trapping in the MoTe$_2$ bilayer with the tellurium vacancy, V$_{Te}$. (a,b) Phonon-driven trapping, process ② in Figure 1(b). (c,d) Trapping driven simultaneously by the Auger and phonon mechanisms, process ④ in Figure 1(c). Blue curves in parts (a, c) show the evolution of electron population in the trap state, while parts (b, d) present the change of electronic energy of carriers. Auger-type energy exchange between charges accelerates the trapping, bringing agreement with the experiment, Figure 2(b). The solid pink circles in (c) depict the THz experimental results at the carrier density of 4.6×10^{20} cm^{-3}. Note that this kinetics trace is reversed vertically in order to show the loss of carrier to trap levels (or increase of electron population in trap level). The dynamics in (d) is not exponential at the beginning because the system needs time to explore the Hilbert space of final states. Only half of the trapped electron energy is transferred to the 2nd electron, with the other half going to phonons.

carrier trapping to ~2 ps, matching very well with the experimental data presented in Figure 2(b). Figure 5(d) demonstrates that only half of the energy lost by the 1st electron during the trapping is deposited into the 2nd electron by the Auger-type scattering (i.e., 0.1 eV). The remaining half of the trapped electron energy is accommodated by phonons (i.e., 0.1 eV from total available energy of 0.2 eV). Figure 5(d) also shows that the Auger-type scattering continues until the 1st electron is fully trapped and with energy fully converted to phonons. The 1st electron energy continues to decrease up to 4.5 ps. The energy of the 2nd electron increases concurrently, and after that the energy decreases due to intraband electron–phonon relaxation. The initial dynamics is not exponential, in particular, since the quantum system needs time to explore the full Hilbert space of available states. The simulation results show that the electron–phonon scattering to the trap levels competes strongly with Auger-type electron–electron scattering, and the overall trapping process can be characterized as an entangled combination of charge–phonon and Auger scattering.

The successful competition of the phonon-mediated electron trapping with the Auger-type electron trapping seen in our simulations can be attributed to the following factors. First, the pure phonon-mediated electron trapping is already quite fast in bilayer MoTe$_2$ (i.e., ~7 to 8 ps), only a factor 2 to 3 slower than the Auger-type trapping. This is because the trap states are relatively shallow, about 0.2 to 0.3 eV below the CBM as shown in Figure 3(b). Occasionally, thermal atomic fluctuations decrease this energy gap even further (see Section V of SI). Besides, as defect density increases, many trap states appear near band edges (see Section VIII of SI). These states speed up phonon-mediated trapping and further compete with Auger trapping. The NAC between electrons in CBM and trap states is slightly larger than the direction recombination of NAC between the electrons in CBM and the holes in VBM as was listed previously in Table 1. Since gaps between trap states and band edges are even smaller in TMDs with high defect concentration (see Section VIII of SI), the NAC for trapping should be even larger than for direct recombination. Second, the other electron that accommodates the trapped electron's

energy during the Auger-type scattering evolves into a dense manifold of CB states (green curve in Figure 5(d)). It undergoes rapid electron–phonon relaxation afterward,[48,71] which is faster than the trapping process itself. The second electron is excited into vibrationally hot electronic states, with fraction of the energy taken by the vibrational degrees of freedom. Third, after the 1st electron starts to get trapped, its charge density gathers around the defect and resides only in one layer, as shown in the inset in Figure 4(b). The localization of the trapped electron weakens its coupling to the free electrons, reducing the efficiency of electron–electron Auger scattering. At the same time, electron localization increases electron–phonon coupling, as evidenced by the larger NAC for the processes involving the trap states as shown in Table 1. The significant contributions of phonons-driven trapping process rationalizes the weaker than quadratic dependence of the trapping rate on the charge carrier density as was observed in our experiments in Figure 2. Our theoretical results indicate that the Auger channel is notably suppressed by the electron trapping channel that deposits electronic energy to phonon modes quickly. The time scale of electron–phonon energy redistribution in the defective crystal does not depend on carrier density. Thus, the lifetime of free charge carriers exhibits very weak carrier density dependence.

In conclusion, we measured charge carrier lifetimes in few-layer 2H-phase MoTe$_2$ with ultrafast optical pump and THz probe transient absorption spectroscopy. Our NAMD and real-time TDDFT calculations show that the observed short carrier lifetime is caused by defects in this system. We find that the Auger process alone cannot explain the weak dependence of the lifetime of photogenerated carriers over a factor of 100 variation of carrier density. An efficient energy dissipation into phonon modes competes successfully with electron–electron scattering, rationalizing the experiments. Intrinsic defects in TMD samples create trap states that are close in energy to band edges, making phonon-driven carrier trapping already quite efficient. During the Auger process, the other electron that accepts the energy of the trapped electron is excited into vibrationally hot states and undergoes rapid intraband electron–phonon relaxation. As a result, half of the trapped

electron energy goes directly into phonons. Further, as electron gets trapped, it localizes around the defect and only resides in one layer, decreasing its coupling to the free delocalized charge carriers. The strong participation of phonons during the trapping process leads us to conclude that charge trapping at high carrier densities occurs by the phonon-suppressed Auger mechanism that shows weaker dependence on charge carrier density than the standard Auger-type charge−charge scattering.

We find that defects play a dual role in charge trapping. At low carrier densities, defects provide an efficient charge relaxation pathway, accelerating nonradiative carrier losses compared to pristine samples. Charge trapping is mediated by phonons in this regime. As the carrier density increases, Auger-type charge−charge scattering becomes important, accelerating carrier trapping. However, instead of the rapid reduction of carrier lifetime with carrier density by the quadratic law, the rate shows a much weaker carrier density dependence because the Auger mechanism is suppressed by active participation of phonons. Our theoretical results show good agreement with the experimental data, provide important mechanistic insights into charge carrier losses in TMDs at the high carrier density, and suggest routes for improving performance of TMD devices.

■ ASSOCIATED CONTENT

ⓢ Supporting Information

The Supporting Information is available free of charge on the ACS Publications website at DOI: 10.1021/acs.nano-lett.9b02005.

> Sample preparation and characterization, experimental layout, THz transition absorption acquisition and data analysis, simulation details, and additional simulation results (PDF)

■ AUTHOR INFORMATION

Corresponding Authors
*E-mail: prezhdo@usc.edu.
*E-mail: bergmann@slac.stanford.edu.

ORCID ⓘ
Linqiu Li: 0000-0001-9564-0577
Xiang Zhang: 0000-0003-4004-5185
Alexander Britz: 0000-0002-1049-2841
Aravind Krishnamoorthy: 0000-0001-6778-2471
Aiichiro Nakano: 0000-0003-3228-3896
Pulickel Ajayan: 0000-0001-8323-7860
Uwe Bergmann: 0000-0001-5639-166X
Oleg V. Prezhdo: 0000-0002-5140-7500

Author Contributions
∇These two authors (L.L. and M.-F.L.) contributed equally.

Notes
The authors declare no competing financial interest.

■ ACKNOWLEDGMENTS

■ REFERENCES

(1) Hong, J.; Hu, Z.; Probert, M.; Li, K.; Lv, D.; Yang, X.; Gu, L.; Mao, N.; Feng, Q.; Xie, L.; Zhang, J.; Wu, D.; Zhang, Z.; Jin, C.; Ji, W.; Zhang, X.; Yuan, J.; Zhang, Z. Exploring atomic defects in molybdenum disulphide monolayers. *Nat. Commun.* **2015**, *6*, 6293.

(2) Brennan, C. J.; Ghosh, R.; Koul, K.; Banerjee, S. K.; Lu, N.; Yu, E. T. Out-of-Plane Electromechanical Response of Monolayer Molybdenum Disulfide Measured by Piezoresponse Force Microscopy. *Nano Lett.* **2017**, *17*, 5464−5471.

(3) Hsieh, K.; Kochat, V.; Zhang, X.; Gong, Y.; Tiwary, C. S.; Ajayan, P. M.; Ghosh, A. Effect of Carrier Localization on Electrical Transport and Noise at Individual Grain Boundaries in Monolayer MoS2. *Nano Lett.* **2017**, *17*, 5452−5457.

(4) Miller, B.; Steinhoff, A.; Pano, B.; Klein, J.; Jahnke, F.; Holleitner, A.; Wurstbauer, U. Long-Lived Direct and Indirect Interlayer Excitons in van der Waals Heterostructures. *Nano Lett.* **2017**, *17*, 5229−5237.

(5) Ganatra, R.; Zhang, Q. Few-Layer MoS2: A Promising Layered Semiconductor. *ACS Nano* **2014**, *8*, 4074−4099.

(6) Lin, Y.-C.; Dumcenco, D. O.; Huang, Y.-S.; Suenaga, K. Atomic mechanism of the semiconducting-to-metallic phase transition in single-layered MoS2. *Nat. Nanotechnol.* **2014**, *9*, 391−396.

(7) Amani, M.; Taheri, P.; Addou, R.; Ahn, G. H.; Kiriya, D.; Lien, D.-H.; Ager, J. W.; Wallace, R. M.; Javey, A. Recombination Kinetics and Effects of Superacid Treatment in Sulfur- and Selenium-Based Transition Metal Dichalcogenides. *Nano Lett.* **2016**, *16*, 2786−2791.

(8) Chia, X.; Ambrosi, A.; Sofer, Z.; Luxa, J.; Pumera, M. Catalytic and Charge Transfer Properties of Transition Metal Dichalcogenides Arising from Electrochemical Pretreatment. *ACS Nano* **2015**, *9*, 5164−5179.

(9) Mannebach, E. M.; Li, R.; Duerloo, K.-A.; Nyby, C.; Zalden, P.; Vecchione, T.; Ernst, F.; Reid, A. H.; Chase, T.; Shen, X.; Weathersby, S.; Hast, C.; Hettel, R.; Coffee, R.; Hartmann, N.; Fry, A. R.; Yu, Y.; Cao, L.; Heinz, T. F.; Reed, E. J.; Dürr, H. A.; Wang, X.; Lindenberg, A. M. Dynamic Structural Response and Deformations of Monolayer MoS2 Visualized by Femtosecond Electron Diffraction. *Nano Lett.* **2015**, *15*, 6889−6895.

(10) Mai, C.; Barrette, A.; Yu, Y.; Semenov, Y. G.; Kim, K. W.; Cao, L.; Gundogdu, K. Many-Body Effects in Valleytronics: Direct Measurement of Valley Lifetimes in Single-Layer MoS2. *Nano Lett.* **2014**, *14*, 202−206.

(11) Bernardi, M.; Palummo, M.; Grossman, J. C. Extraordinary Sunlight Absorption and One Nanometer Thick Photovoltaics Using Two-Dimensional Monolayer Materials. *Nano Lett.* **2013**, *13*, 3664−3670.

(12) Amani, M.; Burke, R. A.; Ji, X.; Zhao, P.; Lien, D.-H.; Taheri, P.; Ahn, G. H.; Kirya, D.; Ager, J. W.; Yablonovitch, E.; Kong, J.; Dubey, M.; Javey, A. High Luminescence Efficiency in MoS2 Grown by Chemical Vapor Deposition. *ACS Nano* **2016**, *10*, 6535−6541.

(13) Voiry, D.; Yang, J.; Chhowalla, M. Recent Strategies for Improving the Catalytic Activity of 2D TMD Nanosheets Toward the Hydrogen Evolution Reaction. *Adv. Mater.* **2016**, *28*, 6197−6206.

(14) Chernikov, A.; Ruppert, C.; Hill, H. M.; Rigosi, A. F.; Heinz, T. F. Population inversion and giant bandgap renormalization in atomically thin WS2 layers. *Nat. Photonics* **2015**, *9*, 466.

(15) Ruppert, C.; Chernikov, A.; Hill, H. M.; Rigosi, A. F.; Heinz, T. F. The Role of Electronic and Phononic Excitation in the Optical Response of Monolayer WS2 after Ultrafast Excitation. *Nano Lett.* **2017**, *17*, 644−651.

(16) Ruppert, C.; Aslan, O. B.; Heinz, T. F. Optical Properties and Band Gap of Single- and Few-Layer MoTe2 Crystals. *Nano Lett.* **2014**, *14*, 6231−6236.

(17) Mak, K. F.; He, K.; Shan, J.; Heinz, T. F. Control of valley polarization in monolayer MoS2 by optical helicity. *Nat. Nanotechnol.* **2012**, *7*, 494.

(18) Wang, H.; Zhang, C.; Chan, W.; Tiwari, S.; Rana, F. Ultrafast response of monolayer molybdenum disulfide photodetectors. *Nat. Commun.* **2015**, *6*, 9831.

(19) Li, L.; Long, R.; Bertolini, T.; Prezhdo, O. V. Sulfur Adatom and Vacancy Accelerate Charge Recombination in MoS2 but by Different Mechanisms: Time-Domain Ab Initio Analysis. *Nano Lett.* **2017**, *17*, 7962−7967.

(20) Zhou, W.; Zou, X.; Najmaei, S.; Liu, Z.; Shi, Y.; Kong, J.; Lou, J.; Ajayan, P. M.; Yakobson, B. I.; Idrobo, J.-C. Intrinsic Structural Defects in Monolayer Molybdenum Disulfide. *Nano Lett.* **2013**, *13*, 2615−2622.

(21) Barja, S.; Refaely-Abramson, S.; Schuler, B.; Qiu, D. Y.; Pulkin, A.; Wickenburg, S.; Ryu, H.; Ugeda, M. M.; Kastl, C.; Chen, C.; Hwang, C.; Schwartzberg, A.; Aloni, S.; Mo, S.-K.; Ogletree, D. F.; Crommie, M. F.; Yazyev, O. V.; Louie, S. G.; Neaton, J. B.; Weber-Bargioni, A. Identifying substitutional oxygen as a prolific point defect in monolayer transition metal dichalcogenides with experiment and theory. *arXiv:1810.03364v1* 2018.

(22) Chen, K.; Ghosh, R.; Meng, X.; Roy, A.; Kim, J.-S.; He, F.; Mason, S. C.; Xu, X.; Lin, J.-F.; Akinwande, D.; Banerjee, S. K.; Wang, Y. Experimental evidence of exciton capture by mid-gap defects in CVD grown monolayer MoSe2. *npj 2D Materials and Applications* **2017**, *1*, 15.

(23) Chen, K.; Roy, A.; Rai, A.; Valsaraj, A.; Meng, X.; He, F.; Xu, X.; Register, L. F.; Banerjee, S.; Wang, Y. Carrier Trapping by Oxygen Impurities in Molybdenum Diselenide. *ACS Appl. Mater. Interfaces* **2018**, *10*, 1125−1131.

(24) Lu, C.-P.; Li, G.; Mao, J.; Wang, L.-M.; Andrei, E. Y. Bandgap, Mid-Gap States, and Gating Effects in MoS2. *Nano Lett.* **2014**, *14*, 4628−4633.

(25) Komsa, H.-P.; Kotakoski, J.; Kurasch, S.; Lehtinen, O.; Kaiser, U.; Krasheninnikov, A. V. Two-Dimensional Transition Metal Dichalcogenides under Electron Irradiation: Defect Production and Doping. *Phys. Rev. Lett.* **2012**, *109*, 035503.

(26) Chow, P. K.; Jacobs-Gedrim, R. B.; Gao, J.; Lu, T.-M.; Yu, B.; Terrones, H.; Koratkar, N. Defect-Induced Photoluminescence in Monolayer Semiconducting Transition Metal Dichalcogenides. *ACS Nano* **2015**, *9*, 1520−1527.

(27) Liu, H.; Zheng, H.; Yang, F.; Jiao, L.; Chen, J.; Ho, W.; Gao, C.; Jia, J.; Xie, M. Line and Point Defects in MoSe2 Bilayer Studied by Scanning Tunneling Microscopy and Spectroscopy. *ACS Nano* **2015**, *9*, 6619−6625.

(28) Rosenberger, M. R.; Chuang, H.-J.; McCreary, K. M.; Li, C. H.; Jonker, B. T. Electrical Characterization of Discrete Defects and Impact of Defect Density on Photoluminescence in Monolayer WS2. *ACS Nano* **2018**, *12*, 1793−1800.

(29) Chen, B.; Sahin, H.; Suslu, A.; Ding, L.; Bertoni, M. I.; Peeters, F. M.; Tongay, S. Environmental Changes in MoTe2 Excitonic Dynamics by Defects-Activated Molecular Interaction. *ACS Nano* **2015**, *9*, 5326−5332.

(30) Hao, K.; Xu, L.; Nagler, P.; Singh, A.; Tran, K.; Dass, C. K.; Schüller, C.; Korn, T.; Li, X.; Moody, G. Coherent and Incoherent Coupling Dynamics between Neutral and Charged Excitons in Monolayer MoSe2. *Nano Lett.* **2016**, *16*, 5109−5113.

(31) Poellmann, C.; Steinleitner, P.; Leierseder, U.; Nagler, P.; Plechinger, G.; Porer, M.; Bratschitsch, R.; Schüller, C.; Korn, T.; Huber, R. Resonant internal quantum transitions and femtosecond radiative decay of excitons in monolayer WSe2. *Nat. Mater.* **2015**, *14*, 889.

(32) Sun, D.; Rao, Y.; Reider, G. A.; Chen, G.; You, Y.; Brézin, L.; Harutyunyan, A. R.; Heinz, T. F. Observation of Rapid Exciton−Exciton Annihilation in Monolayer Molybdenum Disulfide. *Nano Lett.* **2014**, *14*, 5625−5629.

(33) Wang, H.; Zhang, C.; Rana, F. Ultrafast Dynamics of Defect-Assisted Electron−Hole Recombination in Monolayer MoS2. *Nano Lett.* **2015**, *15*, 339−345.

(34) Wang, H.; Strait, J. H.; Zhang, C.; Chan, W.; Manolatou, C.; Tiwari, S.; Rana, F. Fast exciton annihilation by capture of electrons or holes by defects via Auger scattering in monolayer metal dichalcogenides. *Phys. Rev. B: Condens. Matter Mater. Phys.* **2015**, *91*, 165411.

(35) Kar, S.; Su, Y.; Nair, R. R.; Sood, A. K. Probing Photoexcited Carriers in a Few-Layer MoS2 Laminate by Time-Resolved Optical Pump−Terahertz Probe Spectroscopy. *ACS Nano* **2015**, *9*, 12004−12010.

(36) Xing, X.; Zhao, L.; Zhang, Z.; Liu, X.; Zhang, K.; Yu, Y.; Lin, X.; Chen, H. Y.; Chen, J. Q.; Jin, Z.; Xu, J.; Ma, G.-h. Role of Photoinduced Exciton in the Transient Terahertz Conductivity of Few-Layer WS2 Laminate. *J. Phys. Chem. C* **2017**, *121*, 20451−20457.

(37) Docherty, C. J.; Parkinson, P.; Joyce, H. J.; Chiu, M.-H.; Chen, C.-H.; Lee, M.-Y.; Li, L.-J.; Herz, L. M.; Johnston, M. B. Ultrafast Transient Terahertz Conductivity of Monolayer MoS2 and WSe2 Grown by Chemical Vapor Deposition. *ACS Nano* **2014**, *8*, 11147−11153.

(38) Li, L.; Long, R.; Prezhdo, O. V. Why Chemical Vapor Deposition Grown MoS2 Samples Outperform Physical Vapor Deposition Samples: Time-Domain ab Initio Analysis. *Nano Lett.* **2018**, *18*, 4008.

(39) Ziwritsch, M.; Müller, S.; Hempel, H.; Unold, T.; Abdi, F. F.; van de Krol, R.; Friedrich, D.; Eichberger, R. Direct Time-Resolved Observation of Carrier Trapping and Polaron Conductivity in BiVO4. *ACS Energy Letters* **2016**, *1*, 888−894.

(40) Ulbricht, R.; Hendry, E.; Shan, J.; Heinz, T. F.; Bonn, M. Carrier dynamics in semiconductors studied with time-resolved terahertz spectroscopy. *Rev. Mod. Phys.* **2011**, *83*, 543−586.

(41) Jepsen, P. U.; Cooke, D. G.; Koch, M. Terahertz spectroscopy and imaging − Modern techniques and applications. *Laser & Photonics Reviews* **2011**, *5*, 124−166.

(42) Johnston, M. B.; Herz, L. M. Hybrid Perovskites for Photovoltaics: Charge-Carrier Recombination, Diffusion, and Radiative Efficiencies. *Acc. Chem. Res.* **2016**, *49*, 146−154.

(43) Zhang, X.; Jin, Z.; Wang, L.; Hachtel, J. A.; Villarreal, E.; Wang, Z.; Ha, T.; Nakanishi, Y.; Tiwary, C. S.; Lai, J.; Dong, L.; Yang, J.; Vajtai, R.; Ringe, E.; Idrobo, J. C.; Yakobson, B. I.; Lou, J.; Gambin, V.; Koltun, R.; Ajayan, P. M. Low Contact Barrier in 2H/1T′ MoTe2 In-Plane Heterostructure Synthesized by Chemical Vapor Deposition. *ACS Appl. Mater. Interfaces* **2019**, *11*, 12777−12785.

(44) Lin, M.-F.; Kochat, V.; Krishnamoorthy, A.; Bassman, L.; Weninger, C.; Zheng, Q.; Zhang, X.; Apte, A.; Tiwary, C. S.; Shen, X.; Li, R.; Kalia, R.; Ajayan, P.; Nakano, A.; Vashishta, P.; Shimojo, F.; Wang, X.; Fritz, D. M.; Bergmann, U. Ultrafast non-radiative dynamics of atomically thin MoSe2. *Nat. Commun.* **2017**, *8*, 1745.

(45) Sun, Y.; Zhang, J.; Ma, Z.; Chen, C.; Han, J.; Chen, F.; Luo, X.; Sun, Y.; Sheng, Z. The Zeeman splitting of bulk 2H-MoTe2 single crystal in high magnetic field. *Appl. Phys. Lett.* **2017**, *110*, 102102.

(46) Wang, K.; Feng, Y.; Chang, C.; Zhan, J.; Wang, C.; Zhao, Q.; Coleman, J. N.; Zhang, L.; Blau, W. J.; Wang, J. Broadband ultrafast nonlinear absorption and nonlinear refraction of layered molybdenum dichalcogenide semiconductors. *Nanoscale* **2014**, *6*, 10530−10535.

(47) Butscher, S.; Milde, F.; Hirtschulz, M.; Malić, E.; Knorr, A. Hot electron relaxation and phonon dynamics in graphene. *Appl. Phys. Lett.* **2007**, *91*, 203103.

(48) Yang, J.-A.; Parham, S.; Dessau, D.; Reznik, D. Novel Electron-Phonon Relaxation Pathway in Graphite Revealed by Time-Resolved Raman Scattering and Angle-Resolved Photoemission Spectroscopy. *Sci. Rep.* **2017**, *7*, 40876.

(49) Cunningham, P. D.; McCreary, K. M.; Hanbicki, A. T.; Currie, M.; Jonker, B. T.; Hayden, L. M. Charge Trapping and Exciton Dynamics in Large-Area CVD Grown MoS2. *J. Phys. Chem. C* **2016**, *120*, 5819−5826.

(50) Uhd Jepsen, P.; Schairer, W.; Libon, I. H.; Lemmer, U.; Hecker, N. E.; Birkholz, M.; Lips, K.; Schall, M. Ultrafast carrier trapping in microcrystalline silicon observed in optical pump−terahertz probe measurements. *Appl. Phys. Lett.* **2001**, *79*, 1291−1293.

(51) Wang, H.; Zhang, C.; Rana, F. Surface Recombination Limited Lifetimes of Photoexcited Carriers in Few-Layer Transition Metal Dichalcogenide MoS2. *Nano Lett.* **2015**, *15*, 8204−8210.

(52) Hyeon-Deuk, K.; Prezhdo, O. V. Time-Domain ab Initio Study of Auger and Phonon-Assisted Auger Processes in a Semiconductor Quantum Dot. *Nano Lett.* **2011**, *11*, 1845−1850.

(53) Hyeon-Deuk, K.; Prezhdo, O. V. Multiple Exciton Generation and Recombination Dynamics in Small Si and CdSe Quantum Dots: An Ab Initio Time-Domain Study. *ACS Nano* **2012**, *6*, 1239−1250.

(54) Hyeon-Deuk, K.; Kim, J.; Prezhdo, O. V. Ab Initio Analysis of Auger-Assisted Electron Transfer. *J. Phys. Chem. Lett.* **2015**, *6*, 244−249.

(55) Zhu, H. M.; Yang, Y.; Hyeon-Deuk, K.; Califano, M.; Song, N. H.; Wang, Y. W.; Zhang, W. Q.; Prezhdo, O. V.; Lian, T. Q. Auger-Assisted Electron Transfer from Photoexcited Semiconductor Quantum Dots. *Nano Lett.* **2014**, *14*, 1263−1269.

(56) KC, S.; Longo, R. C; Addou, R.; Wallace, R. M; Cho, K. Impact of intrinsic atomic defects on the electronic structure of MoS 2 monolayers. *Nanotechnology* **2014**, *25*, 375703.

(57) Lezama, I. G.; Arora, A.; Ubaldini, A.; Barreteau, C.; Giannini, E.; Potemski, M.; Morpurgo, A. F. Indirect-to-Direct Band Gap Crossover in Few-Layer MoTe2. *Nano Lett.* **2015**, *15*, 2336−2342.

(58) Giannozzi, P.; Baroni, S.; Bonini, N.; Calandra, M.; Car, R.; Cavazzoni, C.; Ceresoli, D.; Chiarotti, G. L; Cococcioni, M.; Dabo, I.; Dal Corso, A.; de Gironcoli, S.; Fabris, S.; Fratesi, G.; Gebauer, R.; Gerstmann, U.; Gougoussis, C.; Kokalj, A.; Lazzeri, M.; Martin-Samos, L.; Marzari, N.; Mauri, F.; Mazzarello, R.; Paolini, S.; Pasquarello, A.; Paulatto, L.; Sbraccia, C.; Scandolo, S.; Sclauzero, G.; Seitsonen, A. P; Smogunov, A.; Umari, P.; Wentzcovitch, R. M QUANTUM ESPRESSO: a modular and open-source software project for quantum simulations of materials. *J. Phys.: Condens. Matter* **2009**, *21*, 395502.

(59) Akimov, A. V.; Prezhdo, O. V. The PYXAID Program for Non-Adiabatic Molecular Dynamics in Condensed Matter Systems. *J. Chem. Theory Comput.* **2013**, *9*, 4959−4972.

(60) Akimov, A. V.; Prezhdo, O. V. Advanced Capabilities of the PYXAID Program: Integration Schemes, Decoherenc:e Effects, Multiexcitonic States, and Field-Matter Interaction. *J. Chem. Theory Comput.* **2014**, *10*, 789−804.

(61) Jaeger, H. M.; Fischer, S.; Prezhdo, O. V. Decoherence-induced surface hopping. *J. Chem. Phys.* **2012**, *137*, 22A545.

(62) Li, L.; Long, R.; Prezhdo, O. V. Charge Separation and Recombination in Two-Dimensional MoS2/WS2: Time-Domain ab Initio Modeling. *Chem. Mater.* **2017**, *29*, 2466−2473.

(63) Long, R.; Prezhdo, O. V. Quantum Coherence Facilitates Efficient Charge Separation at a MoS2/MoSe2 van der Waals Junction. *Nano Lett.* **2016**, *16*, 1996−2003.

(64) Wei, Y.; Li, L.; Fang, W.; Long, R.; Prezhdo, O. V. Weak Donor−Acceptor Interaction and Interface Polarization Define Photoexcitation Dynamics in the MoS2/TiO2 Composite: Time-Domain Ab Initio Simulation. *Nano Lett.* **2017**, *17*, 4038−4046.

(65) Wang, L.; Trivedi, D.; Prezhdo, O. V. Global Flux Surface Hopping Approach for Mixed Quantum-Classical Dynamics. *J. Chem. Theory Comput.* **2014**, *10*, 3598−3605.

(66) Trivedi, D. J.; Wang, L.; Prezhdo, O. V. Auger-Mediated Electron Relaxation Is Robust to Deep Hole Traps: Time-Domain Ab Initio Study of CdSe Quantum Dots. *Nano Lett.* **2015**, *15*, 2086−2091.

(67) Dong, S.; Pal, S.; Lian, J.; Chan, Y.; Prezhdo, O. V.; Loh, Z.-H. Sub-Picosecond Auger-Mediated Hole-Trapping Dynamics in Colloidal CdSe/CdS Core/Shell Nanoplatelets. *ACS Nano* **2016**, *10*, 9370−9378.

(68) Pal, S.; Casanova, D.; Prezhdo, O. V. Effect of Aspect Ratio on Multiparticle Auger Recombination in Single-Walled Carbon Nanotubes: Time Domain Atomistic Simulation. *Nano Lett.* **2018**, *18*, 58−63.

(69) Bhattacharyya, S.; Singh, A. K. Semiconductor-metal transition in semiconducting bilayer sheets of transition-metal dichalcogenides. *Phys. Rev. B: Condens. Matter Mater. Phys.* **2012**, *86*, 075454.

(70) Pan, S.; Ceballos, F.; Bellus, M. Z.; Zereshki, P.; Zhao, H. Ultrafast charge transfer between MoTe2 and MoS2 monolayers. *2D Mater.* **2017**, *4*, 015033.

(71) Butscher, S.; Milde, F.; Hirtschulz, M.; Malic, E.; Knorr, A. Hot electron relaxation and phonon dynamics in graphene. *Appl. Phys. Lett.* **2007**, *91*, 203103.